Journal of Materials Chemistry A



PAPER

View Article Online
View Journal



Cite this: DOI: 10.1039/d5ta06224a

A MXene-derived tetrathiafulvalene metal—organic framework for ultra-long supercapattery

Nasrin Kabeer,^a Yusuf Khan,^{bc} Mostafa Zeama,^a Jehad K. El-Demellawi, ^b Anita Justin,^a Sharath Kandambeth,^a Vinayak S. Kale, ^b Osama Shekhah, ^a Husam N. Alshareef ^b * and Mohamed Eddaoudi *

Metal-organic frameworks (MOFs) have attracted considerable attention for energy-related applications due to their exceptional tailorability, high surface area, and outstanding porosity. However, their widespread deployment in energy storage has been significantly hindered by inherent issues such as low electronic conductivity, chemical instability, and challenging morphological control. In a groundbreaking study, our joint groups first demonstrated the use of V_2CT_x MXenes as a metallic precursor for creating two-dimensional (2D) MOF nanosheets, opening avenues for diverse device applications. Building upon this advancement, we report the synthesis of a conductive tetrathiafulvalene-based 2D MOF that is successfully deployed for supercapattery applications. Our findings reveal that the V_2CT_x -TMOF (T = 4,4',4'',4'''-([2,2'-bi(1,3-dithiolylidene)]-4,4',5,5'-tetrayl)tetrabenzoic acid), synthesized directly from V_2CT_x MXenes with a distinct 2D nanosheet morphology, exhibits one of the finest electrochemical performances with very remarkable long-term cycling stability and high specific capacity. This work presents a novel approach to developing advanced MOF-based electrode materials by leveraging the unique attributes of MXenes precursors.

Received 1st August 2025 Accepted 10th October 2025

DOI: 10.1039/d5ta06224a

rsc.li/materials-a

Introduction

The pursuit of efficient energy storage solutions has become increasingly critical in the context of escalating global energy demands. In this regard, metal-organic frameworks (MOFs), formed through the self-assembly of metal ions and organic linkers, have emerged as outstanding candidates for various energy-related applications due to their exceptional customizable structures, high surface area, and inherent tunable porosity. Nevertheless, the practical application of MOFs is often limited by intrinsic challenges such as their typically low electronic conductivity and poor chemical stability. In contrast, MXenes, a fast-growing family of two-dimensional (2D) materials, offer excellent electrical conductivity stemming from their highly occupied energy states at the Fermi level and metal-like free charge electron density. Since their discovery, MXenes have garnered substantial interest due to their

In a pioneering study by our groups, Wu *et al.*¹² (2019) successfully demonstrated the synthesis of precisely thickness-controlled vanadium porphyrin framework (V-PMOF) nanosheets *via* using tetrakis(4-carboxyphenyl)porphyrin (H₄-TCPP) as an organic linker, and V₂CT_x MXenes as a metal precursor. This seminal work unveiled a previously unexplored and highly effective strategy for the nanoscale construction of derived-MOF architectures directly from MXenes.

combination of uniquely tunable and superior properties, which are associated with their versatile surface chemistry.5-8 MXenes have shown considerable promise in environmental and energy applications.9-11 MXenes are typically produced by exfoliating their parent carbide or nitride ceramics, known as MAX phases. Upon chemical etching, the resulting 2D layered structure of MXenes adheres to the general formula $M_{n+1}X_nT_x$, where T_r represents the suite of surface functional groups, such as -O, -OH, -F, and -Cl. These surface terminal groups (T_x) function as strong electron acceptors, owing to the high work functions and high electron affinity of MXenes. These surface characteristics facilitate the synthesis of MXene-based hybrids, promoting the deprotonation of organic ligands, thereby enabling effective coordination and bridging with underlying metal centres. Meanwhile, these protonated ligands can readily access the abundant reactive sites on the atomically thin and structurally accessible surfaces of the MXene nanosheets, potentially accelerating the coordination process while preserving the underlying layered structure.12

^aFunctional Materials Design, Discovery and Development Research Group (FMD3), Division of Physical Science and Engineering (PSE), King Abdullah University of Science and Technology (KAUST), Thuwal 23955-6900, Kingdom of Saudi Arabia. E-mail: mohamed.eddaoudi@kaust.edu.sa

^bCenter for Renewable Energy and Storage Technologies (CREST), King Abdullah University of Science and Technology, Thuwal, 23955-6900, Saudi Arabia. E-mail: husam.alshareef@kaust.edu.sa

^{*}Materials Science and Engineering, Division of Physical Science and Engineering (PSE), King Abdullah University of Science and Technology (KAUST), Thuwal, 23955-6900, Saudi Arabia

Despite these advancements, expanding the diversity of organic ligands in the chemical transformation synthesis of MXene-derived MOFs remains a key challenge. The rational design and synthesis of novel MOFs incorporating diverse ligands, along with the exploration of more sophisticated fabrication strategies, continue to pose significant challenges in achieving the desired functionalities.13,14 Building upon earlier studies, Tan et al.15 developed MOF@MXene heterostructures by partially transforming V₂CT_x MXenes into MOFs. This approach provided a pathway to integrate conductive MXenes within the MOF. Subsequently, using a metal-ion-assisted transformation strategy, Zhao et al.16 pioneered the synthesis three-dimensional catechol-based TiCu-HHTP MOFs featuring non-interpenetrating SrSi₂ (srs) topologies, employing a metal-ion-assisted transformation strategy. These MOFs were derived from Ti₃C₂T_x MXene precursors using Cu²⁺ ions as coordinating agents. The transformation process involves a synergistic mechanism comprising electron transfer from Ti₃C₂T_x to electrostatically adsorbed Cu²⁺ ions to initiate redox reactions, rupture of Ti-C bonds leading to the release of Ti⁴⁺ ions, and subsequent chelation coordination of Ti⁴⁺/Cu²⁺ with HHTP to form the 3D MOF structure.

Despite these very few advancements, ¹⁷⁻¹⁹ the synthesis of MOFs from MXenes and their applications across diverse fields remain relatively underexplored. Nevertheless, this approach represents a significant advancement, as MXenes, when used as a metal precursor, not only enhance conductivity but also enable the precise control of morphology, resulting in nanosized particles that offer superior properties compared to traditional microcrystalline MOF particles.¹²

Here, in this study, we focus on synthesizing a MXenederived MOF incorporating a conductive core based on a H₄TTF linker (4,4',4",4"'-([2,2'-bi(1,3-dithiolylidene)]-4,4',5,5'tetrayl)tetrabenzoic acid) and V2CTx MXenes as a metal precursor. TTF is a well-known sulfur-rich, π -conjugated organic molecule whose derivatives have been widely employed in designing conductive MOFs, owing to the favourable π - π stacking interactions among TTF moieties. 19,20 Despite these promising features, the application of conductive TTF-based MOFs in hybrid energy storage systems such as supercapatteries remains relatively unexplored. Moreover, many reported TTF-based MOFs suffer from limited electrical conductivity compared to other high-conducting materials, which negatively impacts their electrochemical performance.²¹ To address this challenge, oxidation of TTF into TTF^{*+} radical cations, most commonly achieved through cation doping such as iodine doping, has been demonstrated in the literature to enhance the conductivity of TTF derivatives and thereby improve their electrochemical behavior.20,22

Following the meticulous synthesis and comprehensive physicochemical characterization, the V_2CT_x -based TTF MOF (V_2CT_x -TMOF) has been identified as a highly promising candidate for advanced supercapattery applications. Supercapatteries have garnered significant attention due to their unique ability to combine the high energy density of batteries with the high-power density and rapid charge–discharge capability of supercapacitors, alongside excellent long-term cycling

stability.^{23–26} In recent years, progress in nanostructured material synthesis and innovations in device engineering have accelerated the development of supercapattery technology.^{27–29} Hence, a hybrid supercapattery, which merges the rapid power delivery of supercapacitors with the high energy storage capacity of batteries, is widely regarded as an ideal energy storage system.^{30–32} Substantial research efforts have been dedicated to the development of such hybrid devices, aiming to harness the complementary advantages of both technologies through strategic material and structural design.

Herein, we successfully constructed the desired V₂CT_x-TMOF, which was found to exhibit a robust and densely packed architecture. Notably, the electrochemical performance of our materials has outperformed that of previously reported TTFbased MOFs, even without additional doping or post-synthetic modification. Furthermore, we present a comprehensive analvsis of the pseudocapacitive behaviour and charge storage mechanism of the 2D layered V2CTx-TMOF, which intrinsically possesses a high, well-defined surface area and favourable structural features for enhanced electrochemical performance. In the context of an asymmetric cell design, where activated carbon serves as the anode, we discovered that the V₂CT_r-TMOF significantly outperforms as the cathode, demonstrating excellent pseudocapacitive performance. Specifically, the V₂CT_x-TMOF-based electrode exhibited dominant pseudocapacitive behaviour, retaining an impressive 91% of its initial capacitance after 30 000 galvanostatic cycles at 5 A g⁻¹. Additionally, it achieved a gravimetric capacity of 480 C g⁻¹ at a current density of 1 A g⁻¹, displaying both high capacity and impressive electrochemical stability, positioning it as a highly competitive material for advanced energy storage.

Experimental section

Synthesis of MOFs

Synthesis of V_2CT_x MXenes from V_2AlC . V_2CT_x MXene synthesis was commenced by adding 1 g of V₂AlC MAX phase powder to 20 mL of hydrofluoric acid (HF, 48% Sigma-Aldrich). 12,33 The resulting heterogeneous solution was gently stirred for 24 hours at 35 °C to ensure complete and selective exfoliation of the aluminium (Al) layers. Following the etching process, the resultant acidic solution was subjected to several rounds of centrifugation and decantation using deionized (DI) water until a neutral pH of \sim 6 was achieved. For delamination, 10 mL of 1 M tetramethylammonium hydroxide (TMAOH) was subsequently added to the MXene suspension and stirred for 4 hours at room temperature (RT) to allow for efficient intercalation. Afterward, the suspension of delaminated MXene nanosheets was washed thoroughly using DI water before undergoing a solvent exchange using N,N-dimethylformamide (DMF). The obtained solution has a gravimetric weight of 1 mg mL^{-1} .

Synthesis of the V₂CT_x-TMOF. To synthesize the V₂CT_x-TMOF directly from delaminated MXene solution, 30 mL of a V₂CT_x MXene suspension (1 mg mL⁻¹) in *N*,*N*-dimethylformamide (DMF) was initially sonicated for 5 min to ensure uniform dispersion and prevent agglomeration.

Subsequently, 68 mg of the H₄TTF linker was added gradually to the reaction mixture under continuous stirring. After 30 minutes, 5 mL of glacial acetic acid was added to facilitate the protonation and coordination, and the solution was thoroughly mixed before being transferred to a 50 mL Teflon-lined autoclave. The sealed autoclave was then subjected to solvothermal heating for 24 hours at 180 °C. Following the reaction, the autoclave was allowed to cool naturally to room temperature to ensure controlled crystallization. The resulting brownishorange product was then meticulously collected through centrifugation at 7000 rpm, followed by thorough washing with fresh DMF to remove unreacted species. For comprehensive solvent exchange and purification, the product was subsequently immersed in methanol for 24 hours, ensuring the complete removal of residual solvents and unreacted components. The final highly purified V₂CT_x-TMOF material was obtained by vacuum-assisted filtration at room temperature.

Synthesis of the VOSO₄-TMOF. The synthesis of the VOSO₄-TMOF followed conditions identical to those described for the V₂CT_r-TMOF, with the sole modification of the metal precursor solution. Briefly, 30 mg of vanadium(IV) oxysulfate (VOSO₄) was precisely dissolved in 30 mL of DMF and continuously stirred after adding the H₄TTF linker. Before being subjected to solvothermal reaction at 180 °C, 5 mL of glacial acetic acid was added. The resulting brownish-orange precipitate was washed thoroughly and solvent exchanged using methanol, mirroring the purification steps for the MXene-derived MOF.

Electrode material synthesis

The electrochemical experiment employed a two-reaction setup, one of which is a three-electrode analysis to know the material's electrochemical behaviour, and the other is a full cell supercapattery device by executing an asymmetric cell using activated carbon as the anode.34,35 Normally, the preparation of the electrode material was executed by adding 37.5 mg of V₂CT_x-TMOF as an active material, 10 mg of Super P carbon as a conducting agent, and 2.5 mg of PVDF polymer as a binder in a ratio of 75: 20:5, respectively. All these are thoroughly mixed for 1 hour by grinding in an agate mortar and sealed as the V2CTx-TMOF EM (electrode material) for further use. Similarly, VOSO4-TMOF and activated carbon (AC) electrode materials were also prepared and stored for comparison of the electrochemical activities. 3 M KOH is used as an electrolyte for further studies, and nickel foam is used as a current collector. 3 mg of this electrode material was made into a paste using N-methyl-2-pyrrolidone (NMP) solvent and cast on a nickel foam substrate of 2 \times 4 cm² dimensions.

Results and discussion

Material evolution and characterization

The synthesis begins by producing a suspension of highly delaminated, mono- to few-layered stacks of V2CTx MXene flakes in DMF. Furthermore, for the synthesis of the MOF, this MXene solution is used as the metal precursor solution (Fig. 1). The possibility of using V_2CT_x MXenes as a metal source to

synthesize new MOFs was assessed via the solvothermal reaction with the H₄TTF linker, which was explored and confirmed by PXRD (Fig. 2a). Initially, the successful synthesis of V_2CT_x MXenes was confirmed using a combination of PXRD and SEM measurements. Fig. S1 and S2 depict the corresponding PXRD patterns and SEM of the parent V2AlC MAX phase and etched V_2CT_x MXenes. The observed diffraction peaks and sheet-like morphology after etching and delamination are consistent with the standard pattern obtained for V₂CT_x from the literature. 33,36,37 The obtained V_2CT_x was then employed as the definitive metal precursor for the targeted MOF, and for comparison, we have used VOSO4 as a metal precursor under the same conditions to produce the MOF solvothermally. The V₂CT_x MXenes and other soluble metal salt VOSO₄-derived MOF powders show excellent agreement with the simulated result, suggesting the universality of V₂CT_x MXenes as a metal source in MOF synthesis. Notably, the FWHM of the VOSO₄-TMOF is slightly narrower than that of the V₂CT_x-TMOF, which is due to the larger size of the crystals and may exhibit higher crystallinity compared to nanosheets. However, moderate crystallinity with defect-rich structures is often more advantageous, as it enhances pseudocapacitance while maintaining structural stability. Thus, tailoring crystallinity is crucial and beneficial to ensure structural integrity and controlled defects to maximize active sites and ion accessibility. This is highly consistent with our electrochemical properties of both MOFs. The porosity of the V₂CT_x-TMOF and VOSO₄-TMOF was investigated, and they both exhibit type-I N₂ sorption isotherms (Fig. 2b, S3, and S4). The experimental Brunauer-Emmett-Teller (BET) surface area is 971 m² g⁻¹, indicating the complete conversion of MXenes to MOFs. The theoretical (0.50 cm³ g⁻¹) pore volume well agreed with experimental pore volumes (0.44 cm³ g⁻¹) for the V₂CT_x-TMOF. The average pore sizes are found to be \sim 6.4 Å and \sim 9.7 Å, which is in good agreement with the theoretical crystal structure with two pore channels of average pore sizes 6.7 Å and (9-10.7) Å (Fig. S3).

SEM and TEM images are provided in Fig. 2c-f to reveal the materials' morphology. Unlike the VOSO₄-TMOF (Fig. S7), the MXene-derived MOF, having a nice 2D sheet morphology, was visible. When V₂CT_x nanosheets are converted to the V₂CT_x-TMOF, morphology control from MXenes is retained in this method and is the major highlight of MXene-derived MOFs. This process enables the realization of the MXene effect on the morphology of the MOF synthesis. Generally, conventional MOFs designed by coordination reactions between inorganic metal precursors, such as metal sulphates, chlorides, etc., and organic ligands in polar solvents usually have limited control over the morphology of MOFs with the required dimensionality. While MXenes are used as a metal precursor, the protonated ligands may find sufficient attack sites on the atomically thin MXene surface, which could facilitate the reaction without compromising the underlying 2D architecture of MXenes.12

During the first investigation of a MXene-derived MOF, our group showed that MXenes can be used as a metal source in the synthesis of MOFs with controlled morphologies. In this work, the synthesis of the V2CTx-TMOF with a 2D nanosheet morphology was achieved for the first time. These MOFs with

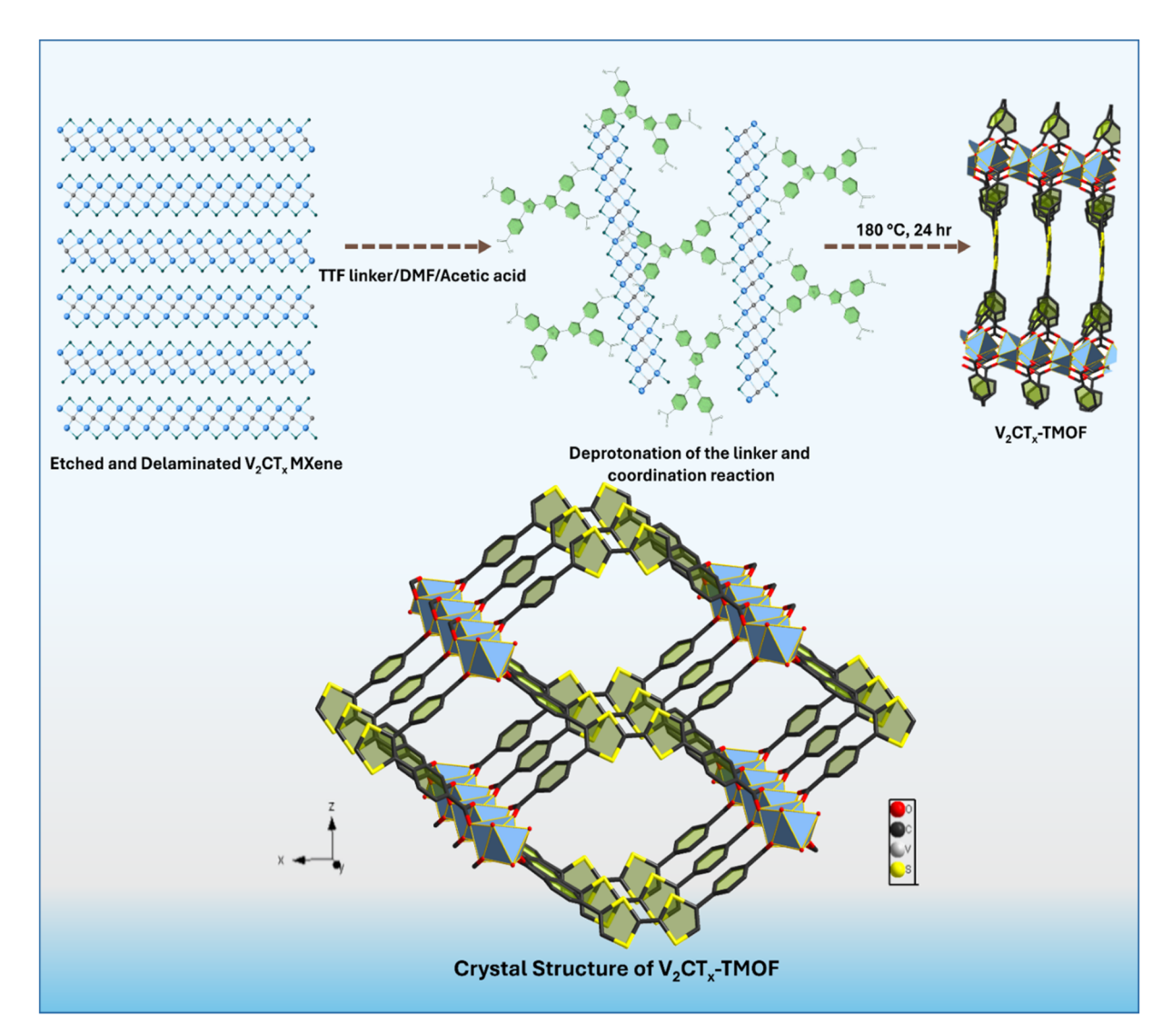


Fig. 1 Schematic representation of the synthesis scheme of the V_2CT_x -TMOF and its structure.

the 2D sheet morphology enable good ion diffusion channel growth and are efficient for providing better electrochemical performance. To understand the difference in MXene-derived MOFs as well as metal salt-derived MOFs, we have compared their performance electrochemically. The V₂CT_x-TMOF can benefit from better electrochemical performance due to its high surface area and good bulk electrical conductivity of 3.8 \times 10⁻⁶ S cm⁻¹, measured using the 4-point probe technique, compared to the VOSO₄-TMOF (3.4 \times 10⁻⁶ S cm⁻¹), which has slightly lower electrical conductivity. Accordingly, this MXenederived thin nanosheet can act as a conductive network during electrochemical application and lead to higher electrochemical properties. Nonetheless, while our measurements confirm the slightly higher intrinsic conductivity of the V₂CT_x-TMOF (3.8 \times 10⁻⁶ S cm⁻¹) compared to the VOSO₄-TMOF (3.4 \times 10⁻⁶ S cm⁻¹), we agree that the primary advantage lies in the morphological effect on the overall electrode architecture. In fact, our claim that the 'thin nanosheet can act as a conductive network' refers to its role within the composite electrode. The 2D morphology of the V₂CT_x-TMOF facilitates a much more

efficient percolating network with the Super P carbon additive. Such planar sheets allow for surface-to-surface contacts, creating continuous electron pathways with reduced tortuosity. This is in stark contrast to the point-to-point contacts formed between the zero-dimensional nanoparticles of the VOSO₄-TMOF, which would result in higher inter-particle and charge-transfer resistances. Therefore, even with similar intrinsic conductivities, the 2D architecture of the MXene-derived MOF is critical for ensuring rapid electron transport throughout the entire electrode volume, enabling superior rate capability and higher utilization of the active material.

To assess the stability of MOFs, we have measured PXRD after sorption analysis (Fig. S5), and the diffraction planes remain unaffected before and after sorption, affirming the higher stability of the material. To elucidate the thermal stability, thermal gravimetric analysis (TGA) was conducted at a heating rate of 5 °C min $^{-1}$ to 800 °C min $^{-1}$ with N $_2$ flow for both synthesized MOFs. The TGA curves (Fig. S6) confirm that both materials are thermally stable until 400 °C with no significant weight loss, providing good stability. This thin

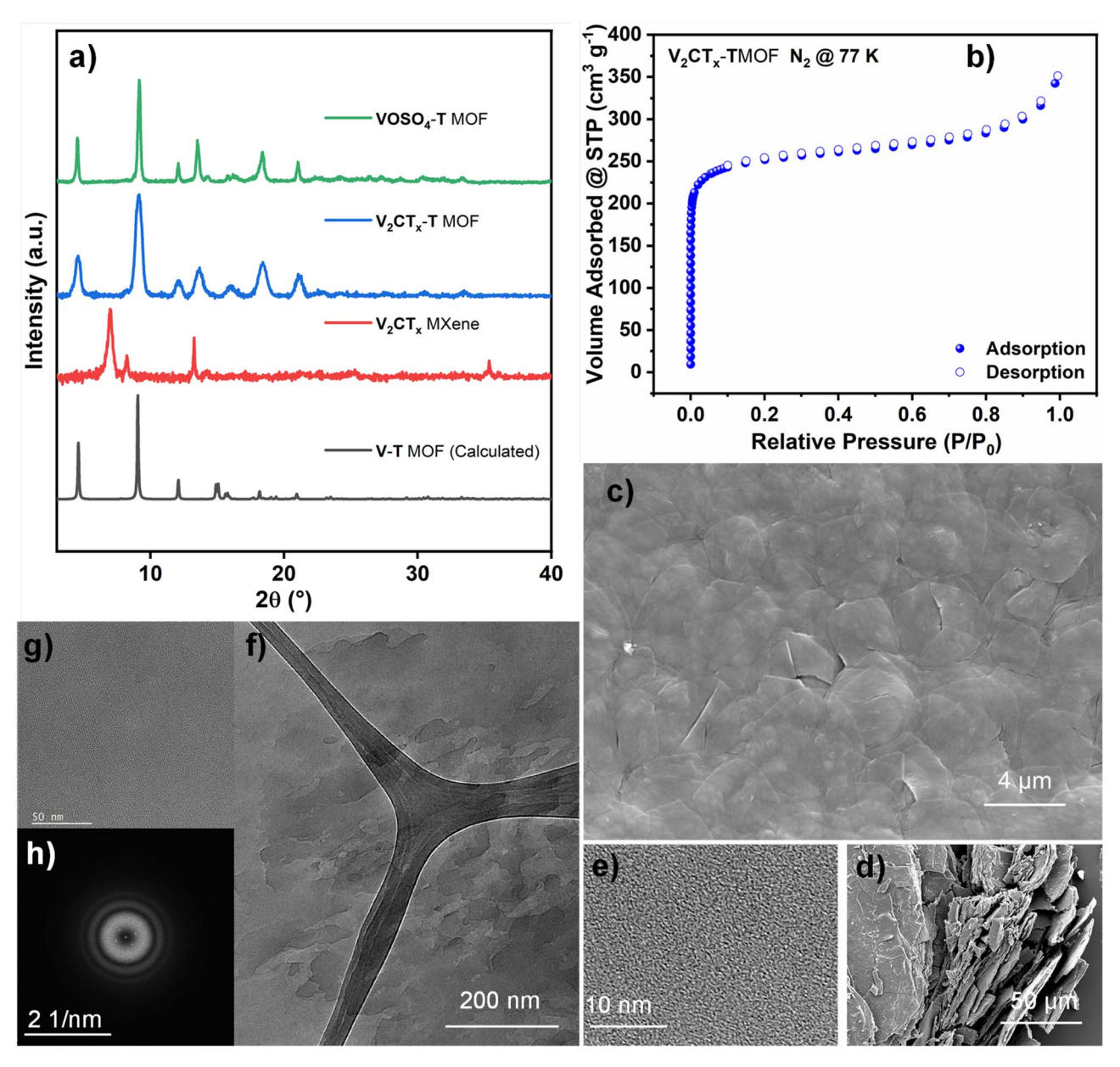


Fig. 2 Characterization studies of the V_2CT_x -TMOF: (a) X-ray diffraction patterns of the simulated V-TMOF (black), V_2CT_x MXene (red), V_2CT_x -TMOF (blue), and VOSO₄-TMOF (green); (b) N_2 adsorption–desorption isotherm of the V_2CT_x -TMOF; (c and d) SEM images of the V_2CT_x -TMO; (e-g) TEM images of the V₂CT_x-TMOF and (h) corresponding SAED pattern.

nanosheet can act as a conductive network during electrochemical application compared to the nanoparticle resulting from the VOSO₄-TMOF. The morphological analysis reveals that the nanosheets are stacked parallel to each other, which enables a higher specific surface area, potentially leading to a larger electrolyte-accessible area, additional electroactive sites, and facile electron transmission, all of which are beneficial for energy storage applications.

Electrochemical characterization of the V₂CT_r-TMOF and its mechanism

Innovative energy storage systems such as supercapatteries, taking advantage of advanced materials design, could manage the escalating energy demands of real-world scenarios. Because of their high power density, quick charge and discharge rate, and extended lifespan, supercapatteries are among the most promising power sources for human needs.38-40 Out of this interest, MOF's large specific surface areas and profusion of redox-active sites have drawn increased interest in energy storage.3,23,41 The three main techniques for evaluating the performance of electrode materials for supercapattery applications are cyclic voltammetry (CV), galvanostatic chargedischarge (GCD), and cycling stability. Depending on the material's nature, each material will exhibit distinct characteristics in the electrochemical mechanism.

To thoroughly assess the behaviour of the V₂CT_x-TMOF, initially, a three-electrode setup is executed and assessed in 3 M KOH electrolyte. The presence of both materials' pseudobehaviour is profound in the CV and GCD curves (Fig. 3a and b) of electrodes coated with the V₂CT_r-TMOF and VOSO₄-TMOF in the potential window of -0.2 to 0.6 V vs. Hg/HgO. To nullify the contribution from the current collector, we have run bare nickel form GCD and CV, which is portrayed along with the materials. Both V-TTF MOFs show distinct redox peaks in the CV as a part of the pseudocapacitance origin. While increasing the scan rate from 5 to 100 mV s⁻¹, the redox nature persists and peak currents increase gradually, indicating good reversibility and fast ion diffusion pathways, which lead to greater storage capacity (Fig. S8a and c). In agreement with the CV analysis, the battery-type redox behaviour is further corroborated by the plateaus observed in the GCD curves.

By evaluating the CV and GCD profiles, it is evident that the MXene-derived MOF exhibits a higher electrochemically active surface area and prolonged charge-discharge times, thus

indicating its superior performance among the two studied MOFs. Despite sharing the same material composition, this enhancement is primarily attributed to their morphological differences. Electrochemically, we have unequivocally demonstrated that the 2D nanosheet morphology of the V₂CT_r-TMOF derived from MXenes provides a higher charge storage ability compared to the nanoparticle morphology of the VOSO₄-TMOF. Consequently, the synthesis strategy of MOFs using MXenes as a precursor is much more appealing for energy-related applications than conventional MOFs. The higher capacity value of the V_2CT_x -TMOF at 1 A g^{-1} current density is 480 C g^{-1} (640 F g^{-1}), whereas for the VOSO₄-TMOF, it is 395 C g^{-1} (526 F g^{-1}). This is superior to the capacitance performance of TTF-based supercapatteries. From the literature, all the studies related to TTF-based supercapatteries are modified with cation doping after material synthesis to mitigate the conductivity issues of the synthesized MOF.20,22 But for the first time, our novel MXene-derived TTF MOF has higher conductivity and good electrochemical behaviour, compared to pristine MXenes

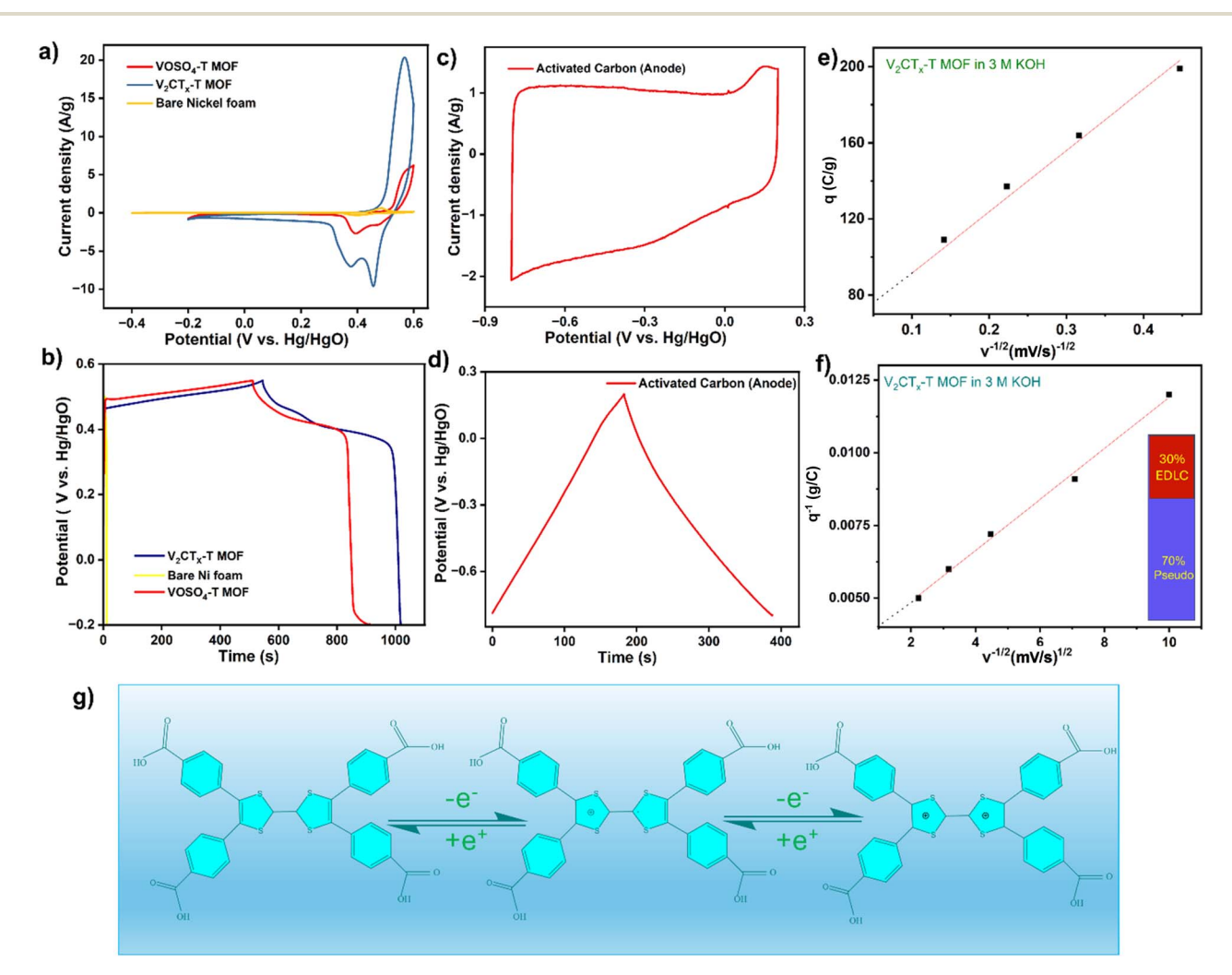


Fig. 3 Electrochemical characterization of the V_2CT_x -TMOF and its mechanism. (a and b) Comparative CV and GCD profiles of the V_2CT_x -TMOF (blue), $VOSO_4$ -TMOF (red), and bare nickel foam current collector (yellow). (c and d) CV and GCD profiles of activated carbon as the anode. (e and f) Trasatti analysis plots to find the capacitive contribution of the V_2CT_x -TMOF and (g) non-faradaic mechanism of the V_2CT_x -TMOF as the electrode material in 3 M KOH.

themselves. All the capacity values are calculated and tabulated in Table S1. To fabricate an asymmetric supercapattery device, we have chosen activated carbon (AC) as an anode, and its electrochemical performance is measured within the potential range of -0.8 to 0.2 V vs. Hg/HgO, and the AC shows a rectangular plateau, promising its electrochemical double-layer charge (EDLC) storage mechanism (Fig. 3c and d). Typically, battery materials show distinct faradaic redox peaks in their CV curves, whereas EDLC materials exhibit a rectangular profile devoid of redox peaks.42 The specific capacity calculated for activated carbon is 225 F g^{-1} , 212 F g^{-1} , 180 F g^{-1} , and 165 F g^{-1} at current densities of 0.5, 1, 5, and 10 A g⁻¹ (Fig. S8b and d). Trasatti analysis^{2,20} was employed to quantitatively deconvolve the capacitance of the V₂CT_x-TMOF, specifically assessing the scan rate dependence of its electrochemical response (Fig. 3e and f). From the analysis, it was found that 70% of the total current was made up of pseudocapacitive contribution, with the capacitive effect gradually increasing at higher scan rates.

According to Trasatti's analysis, the majority of charge storage mechanisms rely on the outer surface pseudocapacitance of the total charge, which is in line with the mechanism of the H₄TTF moiety in the synthesized V₂CT_x-TMOF (Fig. 3g). H₄TTF molecules are conjugated organic compounds with exceptional redox characteristics. They will undertake two consecutive one-electron redox processes, demonstrating good thermodynamic and electrochemical stability.43 Here, H4TTF undergoes two single-electron reactions. During the first redox reaction, H₄TTF releases one electron, yielding a carbon radical (TTF'+), which can be further

oxidized to afford TTF2+. In contrast, for supercapatteries, unlike a bulk non-faradaic mechanism like that of a battery, we cannot expect a pronounced diffusion-controlled process. Instead, a fast surface pseudo-reaction can be available in the charge storage mechanism.

Supercapattery device performance of the V₂CT_x-TMOF

Using the V₂CT_r-TMOF as the positive electrode and AC as the negative electrode, a hybrid supercapattery device was fabricated (Fig. 4a). The positive electrode displays a reversible redox reaction like that of a battery, while the process in the negative electrode is based on the EDLC behaviour concept with electrostatic charge storage. The charge on the positive and negative electrodes must be balanced to fabricate a fully functional hybrid energy storage device. The optimal mass loading of anode and cathode materials was calculated using the following formulae:,42

$$q_+ = Q_+ \times m_+ \tag{1}$$

$$q_{-} = Q_{-} \times m_{-} \tag{2}$$

$$\frac{m_{+}}{m_{-}} = \frac{Q_{-}}{Q_{+}} \tag{3}$$

where the charges held on the positive and negative electrodes are denoted by the symbols q_+ and q_- , respectively, and masses and specific capacities are denoted by m_+ , Q_+ , m_- , and Q_- .

The CV and CD profiles (Fig. 4b and S9) of the constructed asymmetric supercapattery at various cell potentials ranging

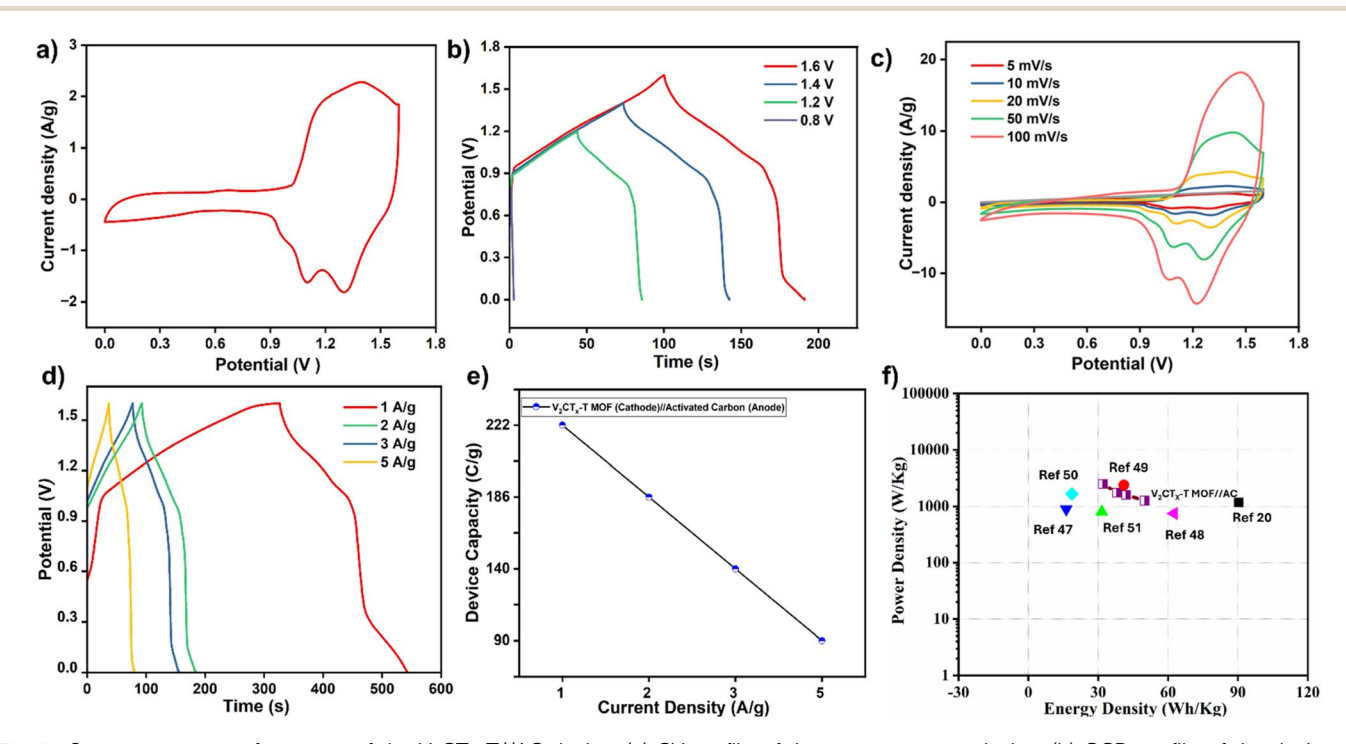


Fig. 4 Supercapattery performance of the V₂CT_x-T//AC device. (a) CV profile of the supercapattery device. (b) GCD profile of the device at different potentials from 0.8-1.6 V. (c and d) CV and GCD curves at variable scan rates and current densities of the supercapattery device. (e) Plot of current density vs. total device capacity. (f) Ragone plot illustrating specific energy and specific power densities of the V₂CT_x-T//AC supercapattery device. 20,47-51

Table 1 Comparative supercapattery performance of the V_2CT_x -T//AC device with available literature data

| Material | Central metal Electrolyte | Electrolyte | Specific capacity without oxidative doping | Specific capacity after oxidative doping Cycle life | Cycle life | Potential window from GCD | Ref. |
|--|-------------------------------------|-------------|---|---|-------------------|------------------------------|-----------|
| $[\operatorname{Cu}(\operatorname{bpp})_2(\operatorname{H}_2\operatorname{O})_2]_n \cdot 2n(\operatorname{HL})$ $[\operatorname{Zn}(\operatorname{py-TTF-py})(\operatorname{BPDC})] \cdot 2\operatorname{H}_2\operatorname{O}$ | Cu Zn oxidative | КОН КОН | 35 C g^{-1} 150 C g^{-1} | $^{}$ 833 C g $^{-1}$ | — 82% over 10k | 0.45 V 0.4 V | 45 20 |
| $\left[(\mathrm{CuCN})_2(\mathrm{TTF}(\mathrm{py})_4) \right]$ | doping with I_2 Cu oxidatively | КОН | $130~{\rm C~g^{-1}}$ | 677.5 C g^{-1} | 81% over 5k | 0.35 V | 22 |
| V_2CT_x -TMOF | $\frac{1}{2}$ | КОН | $480 \text{ C g}^{-1} (640 \text{ F g}^{-1})$ | I | 91% over 30k | 0.75 V | This work |

from 1 to 1.6 V are given to fully understand the stability of the device over higher potentials. Without any electrolyte decomposition, the device clearly demonstrates that a maximum cell potential of 1.6 V may be achieved in an aqueous KOH electrolyte. Therefore, the cell potential was set at 1.6 V for subsequent experiments. The device CV and GCD profiles at various scan rates and current densities are displayed in Fig. 4c and d. The plateau shows a quasi-rectangular shape, indicating the predominant capacitive character of the device.44 It retains its shape as the scan rate is increased, which is evidence of the device's high-rate capacity. In Fig. 4e and f, the performance of the device is summarized as a device capacity vs. current density plot and a Ragone plot after calculating specific energy and power densities. The device showed a greater specific capacity of 888 C g^{-1} (525 F g^{-1}) at 1 A g^{-1} current density, which is well in agreement with three electrode measurements. Total capacitance of the device is calculated as follows: 222, 185, 170, and 144 C g^{-1} at 1, 2, 3, and 5 A g^{-1} , respectively. When the current density gradually increases, the device capacity remains quite stable, 65% of the initial capacitance (144 C g⁻¹), indicating the high-capacity retention of the hybrid device. The V₂CT_x-TMOF// AC hybrid device produced 1264 W kg⁻¹ of specific power and a remarkably high specific energy of 50 Wh kg⁻¹. The specific energy density of 32 Wh kg⁻¹ was sustained even at a high specific power density of 2504 W kg⁻¹. The obtained specific energy and specific power of the V₂CT_r-TMOF//AC supercapattery device are displayed in detail in Table S2. Here, V2CTx-TMOF pseudocapacitance linked to reversible intercalation and de-intercalation of electrolyte ions contributes to the capacitance's superior performance in this system, along with activated carbon's EDLC mechanism on the other electrode. It is evident from the literature^{20,22,45} (Table 1) that the V₂CT_x-TMOF hybrid device has equivalent performance to the cation-doped TTF-based systems and has superior performance to pristine TTF supercapattery systems.

Long cycling analysis and comparison of results

For real-time applications, cycling stability is a crucial prerequisite for electrode materials. Because of volumetric changes caused by the ongoing redox reaction on the surface of EM and the possibility of MOF structure destruction for long-term usage, they can generally lose stability. So, the primary problem with this kind of battery-type electrode material is its poor cycle stability. 46 But here, this 2D multilayer morphology can help reduce the volumetric fluctuations during the cycling process. The long-term cycling stability of the supercapattery device up to 30 000 cycles at a current density of 5 A g⁻¹ is available in Fig. 5a. Additionally, the device's GCD profile at some initial and final cycles on reaching 30 000 cycles is displayed in Fig. S10. A 91% capacity retention with 100% coulombic retention, even after 30 000 consecutive cycles of charging and discharging, could be a great advantage of this material. From the literature, it is visible that no such system surpasses 10 000 cycles with higher stability (Table 1).

Additionally, electrochemical impedance spectroscopy (EIS) studies were carried out in the 10 mHz to 100 kHz frequency

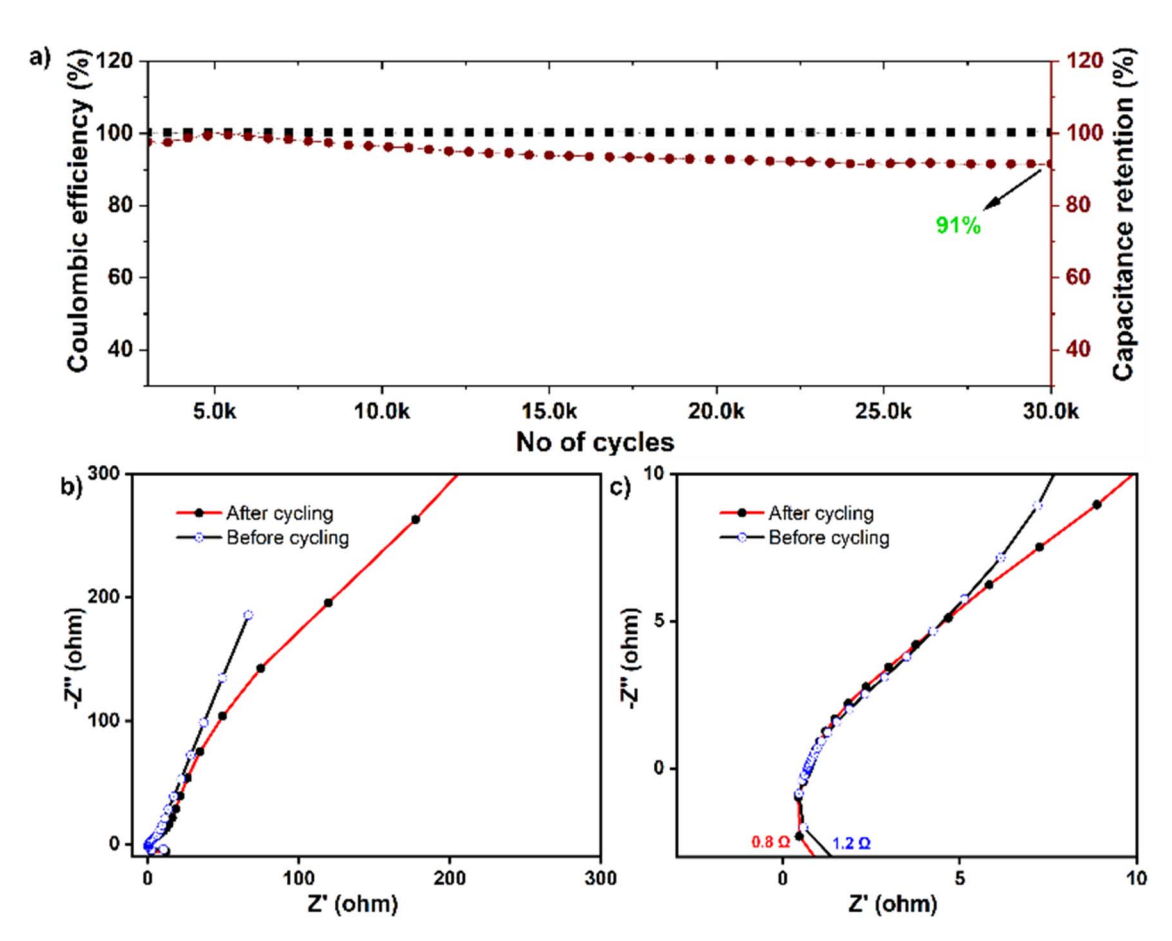


Fig. 5 (a) Cycling stability of the V_2CT_x -T//AC supercapattery device up to 30 000 cycles with coulombic efficiency and capacitance retention. (b and c) EIS-Nyquist plots before and after cycling analysis with an enlarged view of the lower frequency region.

range. A Nyquist plot was drawn to explore the EIS data. The Nyquist plot of the supercapattery before and after 30 000 cycles is shown in Fig. 5b and c. Before cycling, the solution resistance (R_s) of the V_2CT_x -T//AC hybrid device was 0.8 Ω and 1.2 Ω , respectively. Similarly, before and after 30 000 cycles, the charge transfer resistance (R_{ct}) also has a negligible difference, only indicating that the device's resistivity changes are well aligned with the 91% capacitance retention after the cycling. When MXene-derived TTF-based MOFs were employed for energy storage, the results were promising and among the best. The construction of a supercapattery device for practical uses was prompted by this higher performance. The key and impactful findings of this work can be concisely summarized as follows:

(i) On continuation of our group discovery on MXene-derived MOF synthesis, here we have developed a new V_2CT_x -TMOF with precisely controlled 2D morphology, demonstrating a significant advancement in MOF synthesis strategies. (ii) The developed synthesis strategy shows that the inherent metallic properties and 2D architecture of V₂CT_x MXene nanosheets contribute significantly to the enhanced electrical conductivity of the new MOF and its distinct 2D morphology, providing a clear and distinct advantage over the conventionally solvothermally synthesized VOSO₄-TMOF, facilitating rapid electron transport both in-plane (along the MOF sheets) and out-ofplane (between the stacked sheets), thereby promoting efficient charge transfer. (iii) This unique and optimized morphology provides a high specific surface-to-volume ratio and excellent diffusion pathways, which are critical and indispensable for efficient and rapid energy storage mechanisms. Furthermore, the selective incorporation of a redox-active TTF moiety as a structural linker improves the overall device capacity through a straightforward non-faradaic pseudocapacitive charge storage mechanism involving the reversible redox transitions of the TTF units.

Conclusions

We have successfully demonstrated a highly efficient and exceptionally stable V₂CT_x-TMOF-based supercapattery, powered by an optimized electrode nanoarchitecture developed through an improved and advanced method that utilizes V₂CT_x MXenes as a direct MOF precursor. This innovative approach not only significantly broadens the scope of applicable MXene metal precursors but also substantially expands the range of suitable organic ligands, thereby offering broad applicability for the controlled synthesis of MOFs with tailorable morphology and enhanced properties. The synergetic transformation mechanism involves a continuous chelation between in situ generated V^{4+} ions and H_4 TTF ligands, followed by a slow rupture of the V–C bonds, which gradually release V^{4+} ions into the reaction solution. This controlled, slow-release process underpins the morphology-driven synthesis of stable 2D nanosheets of MOFs, ultimately leading to a higher electrochemical surface area and enhanced redox activity, both of which are pivotal for the superior performance of the supercapattery device.

Notably, the carefully designed 2D MOF structure inherently enhances pseudocapacitive behavior, thereby boosting the overall electrochemical performance and specific capacity. Due to their continuous 2D sheet structure, V₂CT_r-TMOFs exhibit a substantially improved electrolyte-accessible surface area and superior intrinsic conductivity. Compared to conventionally synthesized VOSO₄-TMOFs and previously reported TTF-based MOFs, the optimized V₂CT_x-TMOF demonstrates a remarkable specific capacity of 480 C g^{-1} in KOH electrolyte at a current density of 1 A g⁻¹. Its performance is particularly noteworthy, demonstrating superior rate capability and exceptional longterm cycling stability over an unprecedented 30 000 cycles. Moreover, the assembled supercapattery device delivers a significantly enhanced energy density of 50 Wh kg⁻¹ at a higher power density of 2504 W kg⁻¹, showcasing its excellent practical applicability. This work not only establishes a highperformance platform for advanced electrochemical energy storage but also offers invaluable mechanistic insights and rational guidance for designing next-generation energy storage systems through innovative MXene-derived MOF synthesis strategies.

Conflicts of interest

There are no conflicts to declare.

Data availability

The data that support the findings of this work are available from the corresponding author upon reasonable request. The data supporting this article has been included as part of the supplementary information (SI). Supplementary information: figures and tables; experimental procedures; electrochemical calculations; material characterization; and electrochemical characterization. See DOI: https://doi.org/10.1039/d5ta06224a.

Acknowledgements

This work was financially supported by King Abdullah University of Science and Technology (KAUST) under award no. URF/1/5066-01-01.

Notes and references

- K. W. Nam, S. S. Park, R. dos Reis, V. P. Dravid, H. Kim,
 C. A. Mirkin and J. F. Stoddart, *Nat. Commun.*, 2019, 10(1),
- 2 G. Lee, G. Park and S. S. Park, J. Am. Chem. Soc., 2024, 146(43), 29767-29772.

- 3 M. Hmadeh, Z. Lu, Z. Liu, F. Gándara, H. Furukawa, S. Wan, V. Augustyn, R. Chang, L. Liao, F. Zhou, E. Perre, V. Ozolins, K. Suenaga, X. Duan, B. Dunn, Y. Yamamto, O. Terasaki and O. M. Yaghi, *Chem. Mater.*, 2012, 24(18), 3511–3513.
- 4 T. Yang, Y. Yan, R. Liu, K. Huang, R. Xu, J. Chen, J. Tu, S. Liu, L. Kang, Z. Wang, J. Cao and J. Qi, *Nano Lett.*, 2025, 25(19), 7707–7715.
- 5 Y. Gogotsi, Chem. Mater., 2023, 35(21), 8767-8770.
- 6 Y. Zhang, Y. Wang, Q. Jiang, J. K. El-Demellawi, H. Kim and H. N. Alshareef, *Adv. Mater.*, 2020, 32(21), 1908486.
- 7 J. K. El-Demellawi, S. Lopatin, J. Yin, O. F. Mohammed and H. N. Alshareef, ACS Nano, 2018, 12(8), 8485–8493.
- 8 M. Mustakeem, J. K. El-Demellawi, M. Obaid, F. Ming, H. N. Alshareef and N. Ghaffour, *ACS Appl. Mater. Interfaces*, 2022, **14**(4), 5265–5274.
- K. Nasrin, V. Sudharshan, K. Subramani, M. Karnan and M. Sathish, *Small*, 2022, 18(4), 2106051.
- 10 B. Xu and Y. Gogotsi, Adv. Funct. Mater., 2020, 30(47), 2007011.
- 11 Y. Khan, V. S. Kale, J. K. El-Demellawi, Y. Lei, W. Zhao, S. Kandambeth, P. T. Parvatkar, O. Shekhah, M. Eddaoudi and H. N. Alshareef, *Mater. Today Energy*, 2024, 44, 101636.
- 12 H. Wu, M. Almalki, X. Xu, Y. Lei, F. Ming, A. Mallick, V. Roddatis, S. Lopatin, O. Shekhah, M. Eddaoudi and H. N. Alshareef, *J. Am. Chem. Soc.*, 2019, **141**(51), 20037–20042.
- 13 M. Eddaoudi, D. F. Sava, J. F. Eubank, K. Adil and V. Guillerm, *Chem. Soc. Rev.*, 2015, 44(1), 228–249.
- 14 M. G. Lee, S. Kandambeth, X. Y. Li, O. Shekhah, A. Ozden, J. Wicks, P. Ou, S. Wang, R. Dorakhan, S. Park, P. M. Bhatt, V. S. Kale, D. Sinton, M. Eddaoudi and E. H. Sargent, J. Am. Chem. Soc., 2024, 146(20), 14267–14277.
- Y. Tan, L. Yang, D. Zhai, L. Sun, S. Zhai, W. Zhou, X. Wang,
 W. Q. Deng and H. Wu, Small, 2022, 18(50), 2204942.
- 16 W. Wang, Y. Bai, P. Yang, S. Yuan, F. Li, W. Zhao, B. Jin, X. Zhang, S. Liu, D. Yuan and Q. Zhao, *Sci. Bull.*, 2023, 68, 2180–2189.
- 17 L. Sun, J. Sun, S. Zhai, T. Dong, H. Yang, Y. Tan, X. Fang, C. Liu, W. Q. Deng and H. Wu, Adv. Energy Mater., 2022, 12(23), 2200113.
- 18 G. Zhao, H. Lv, Y. Zhou, X. Zheng, C. Wu and C. Xu, *ACS Appl. Mater. Interfaces*, 2018, **10**(49), 42925–42932.
- 19 N. Kitchamsetti and J. S. Cho, J. Energy Storage, 2024, 80, 110293.
- 20 Z. H. Ren, Z. R. Zhang, L. J. Ma, C. Y. Luo, J. Dai and Q. Y. Zhu, ACS Appl. Mater. Interfaces, 2023, 15(5), 6621–6630.
- 21 Y. Zhang, Z. W. Xia, L. J. Shen, H. Tang, X. F. Luo, X. Li and X. Xiao, *ChemComm*, 2023, 59(76), 11429–11432.
- 22 Z. R. Zhang, Z. H. Ren, C. Y. Luo, L. J. Ma, J. Dai and Q. Y. Zhu, *Inorg. Chem.*, 2023, **62**(11), 4672–4679.
- 23 G. Zou, Z. Tian, V. S. Kale, W. Wang, S. Kandembeth, Z. Cao, J. Guo, J. Czaban-Jóźwiak, L. Cavallo, O. Shekhah, M. Eddaoudi and H. N. Alshareef, *Adv. Energy Mater.*, 2023, 13(7), 2203193.
- 24 N. Tang, H. You, M. Li, G. Z. Chen and L. Zhang, *Nanoscale*, 2018, **10**(44), 20526–20532.

- 25 H. Shao, N. Padmanathan, D. McNulty, C. O'Dwyer and K. M. Razeeb, ACS Appl. Mater. Interfaces, 2016, 8(42), 28592-28598.
- 26 X. Wang, R. Zhou, C. Zhang, S. Xi, M. W. M. Jones, T. Tesfamichael, A. Du, K. Gui, K. Ostrikov and H. Wang, J. Mater. Chem. A, 2020, 8(18), 9278-9291.
- 27 M. Hu, H. Zhang, T. Hu, B. Fan, X. Wang and Z. Li, Chem. Soc. Rev., 2020, 49(18), 6666-6693.
- 28 D. Chen, K. Jiang, T. Huang and G. Shen, Adv. Mater., 2020, 32(5), 1901806.
- 29 S. G. Krishnan, A. Arunachalam, P. Jagadish and M. Khalid, 2D Materials for Supercapacitor and Supercapattery Applications, in Adapting 2D Nanomaterials for Advanced Applications, ACS Symposium Series, 2020, ch. 2, vol. 1353, pp. 33-47.
- 30 Z. S. Iro, Int. J. Electrochem. Sci., 2016, 11(12), 10628-10643.
- 31 G. Z. Chen, Int. Mater. Rev., 2017, 62, 173-202.
- 32 Z. Yu, L. Tetard, L. Zhai and J. Thomas, Energy Environ. Sci., 2015, 8(13), 702-730.
- 33 M. Wu, B. Wang, Q. Hu, L. Wang and A. Zhou, Materials, 2018, 11(11), 2112.
- 34 A. Borenstein, O. Hanna, R. Attias, S. Luski, T. Brousse and D. Aurbach, J. Mater. Chem. A, 2017, 5(25), 12653-12672.
- 35 J. Jiang, Y. Zhang, P. Nie, G. Xu, M. Shi, J. Wang, Y. Wu, R. Fu, H. Dou and X. Zhang, Adv. Sustainable Syst., 2018, 2(1), 1700110.
- 36 W. Wu, C. Wang, C. Zhao, D. Wei, J. Zhu and Y. Xu, J. Colloid Interface Sci., 2020, 580, 601-613.
- 37 D. B. Velusamy, J. K. El-Demellawi, A. M. El-Zohry, A. Giugni, S. Lopatin, M. N. Hedhili, A. E. Mansour, E. Di Fabrizio, O. F. Mohammed and H. N. Alshareef, Adv. Mater., 2019, 31(32), 1807658.
- 38 D. P. Dubal, O. Ayyad, V. Ruiz and P. Gómez-Romero, Chem. Soc. Rev., 2015, 44(7), 1777-1790.

- 39 Z. Yang, J. Zhang, M. C. W. Kintner-Meyer, X. Lu, D. Choi, J. P. Lemmon and J. Liu, Chem. Rev., 2011, 111(5), 3577-3613.
- 40 E. Pomerantseva and Y. Gogotsi, Nat. Energy, 2017, 2(7),
- 41 S. Kandambeth, J. Jia, H. Wu, V. S. Kale, P. T. Parvatkar, J. Czaban-Jóźwiak, S. Zhou, X. Xu, Z. O. Ameur, E. Abou-Hamad, A. H. Emwas, O. Shekhah, H. N. Alshareef and M. Eddaoudi, Adv. Energy Mater., 2020, 10(38), 2001673.
- 42 K. Nasrin, K. Subramani, M. Karnan and M. Sathish, J. Colloid Interface Sci., 2021, 600, 264-277.
- 43 X. Wang, A. Lashgari, R. Siwakoti, R. K. Gautam, J. J. McGrath, P. Sarkar, G. Naber, J. Chai and J. J. Jiang, J. Mater. Chem. A, 2023, 11(35), 19056-19065.
- 44 Y. Gogotsi and R. M. Penner, ACS Nano, 2018, 12(3), 2081-2083.
- 45 Z. Y. Zhou, C. Y. Ge, M. Jiang, J. Le Hou, Q. Y. Zhu and J. Dai, Dalton Trans., 2021, 50(32), 11091-11098.
- 46 T. Mao, S. Wang, X. Wang, F. Liu, J. Li, H. Chen, D. Wang, G. Liu, J. Xu and Z. Wang, ACS Appl. Mater. Interfaces, 2019, 11(19), 17742-17750.
- 47 A. A. Bhoite, K. V. Patil, R. S. Redekar, P. S. Patil, V. A. Sawant and N. L. Tarwal, J. Solid State Chem., 2023, 326, 124192.
- 48 C. Li, J. Wang, Y. Yan, P. Huo and X. Wang, Chem. Eng. J., 2022, 446, 137108.
- 49 M. Shaheen, M. Z. Igbal, M. W. Khan, S. Siddique, S. Aftab and S. M. Wabaidur, Energy Fuels, 2023, 37(5), 4000-4009.
- 50 P. Dubey, V. Shrivastav, P. H. Maheshwari, M. Hołdyński, A. Krawczyńska and S. Sundriyal, J. Energy Storage, 2023, 68, 107828.
- 51 S. Gao, Y. Sui, F. Wei, J. Qi, Q. Meng and Y. He, J. Mater. Sci., 2018, 53(9), 6807-6818.